

Disentangling Vortex-driven Dynamics in the Solar Atmosphere Using Information Theory

SUZANA S. A. SILVA,¹ ERICO L. REMPEL,² GARY VERTH,³ ISTVAN BALLAI,³ AND VIKTOR FEDUN¹

¹*Plasma Dynamics Group, School of Electrical and Electronic Engineering, University of Sheffield, Sheffield, S1 3JD, UK*

²*Department of Mathematics, Aeronautics Institute of Technology, Praça Marechal Eduardo Gomes 50, 12228-900, São José dos Campos, SP, Brazil*

³*Plasma Dynamics Group, School of Mathematical and Physical Sciences, University of Sheffield, Sheffield S3 7RH, UK*

ABSTRACT

Solar tornadoes are believed to influence plasma dynamics and create conditions for heating, yet a direct quantitative link is lacking. Here, for the first time, we directly measure vortex-driven dynamics using information-theoretic diagnostics in a Bifrost simulation. By combining Shannon Entropy (SE) and Normalized Mutual Information (NMI), we track how vortices restructure plasma–magnetic interactions and channel energy into heat. The vortex flow originates in the upper photosphere and extends into the chromosphere and upper atmosphere. Relative to a control region dominated by shear flows and transient swirls, the coherent vortex shows stronger statistical interdependence between vorticity and other MHD variables. SE shows that vertical magnetic field entropy increases at the vortex onset as magnetic flux is redistributed, then decreases as the field becomes ordered. Magnetic shear and magnetic energy entropy peak during vortex development, reflecting current and energy build-up. In the upper atmosphere, low entropy in temperature and pressure alongside high entropy in density indicates ordered thermal and pressure fields but irregular mass distribution, a departure from ideal-gas behavior confirmed by weakened temperature–density coupling. NMI shows that temperature couples to different heating drivers with height: compression and vorticity (viscous heating, since vorticity traces velocity gradients) in the lower atmosphere, and vorticity plus magnetic shear in the upper atmosphere (viscous and current-driven heating). Although the simulation does not include explicit physical dissipation, hyperdiffusivity acts on sharp gradients and mimics these processes. Our results demonstrate that vortices drive multiscale coupling between flows and fields, locally shaping solar atmospheric dynamics and heating.

Keywords: Solar chromospheric heating, Quiet Sun, Solar granulation

1. INTRODUCTION

The solar atmosphere supports a variety of vortices, from small-scale along intergranular lanes (Giagkiozis et al. 2018; Silva et al. 2020) to large vortical structures observed at the supergranular junctions (Requerey et al. 2017; Silva et al. 2018; Chian et al. 2019). The intergranular vortices may hit the upper atmosphere, displaying larger rotational signatures in the CaII and H α core lines (Wedemeyer-Böhm et al. 2012; Dakanalis et al. 2021, 2022) known as chromospheric swirls. Wedemeyer-Böhm et al. (2012) traced observa-

tional signatures of vortices across the solar atmosphere showing that they form a structure called solar tornadoes. Silva et al. (2024b) identified that solar tornadoes are, in fact, composed of three co-spatial vortices: a classical flow vortex (the kinetic vortex Silva et al. (2021)), a magnetic vortex consisting of coherent twisted magnetic fields, and a Poynting flux vortex, characterized by swirling trajectories of energy flow.

Numerical simulations have revealed a range of physical processes operating within vortex tubes. In high-plasma- β layers, hydrodynamic flows can twist magnetic fields (Silva et al. 2021), generating magnetic shear and launching torsional waves (Fedun et al. 2011; Yadav et al. 2021). In contrast, in low- β chromospheric regions, the dynamics can become magnetically dominated, with the magnetic field exerting control over plasma motions

through magnetic tension and Lorentz forces (Silva et al. 2022, 2024a). Several studies have also highlighted the development of thin current sheets and localized heating at vortex boundaries, suggesting that magnetic shear and current dissipation may be central to vortex-related heating (Yadav et al. 2021; Silva et al. 2021). Vortices have also been linked to increased electromagnetic energy and plasma heating (Kuniyoshi et al. 2023, 2024; Silva et al. 2024a,b; Przybylski et al. 2025).

While previous studies have demonstrated that vortices in the solar atmosphere often coincide spatially and temporally with magnetic field concentrations, plasma heating, shock and jet formation (e.g., Requerey et al. 2017; Tziotziou et al. 2023; Díaz-Castillo, S. M. et al. 2024), such associations remain largely qualitative. That is, they identify correlations based on collocation or apparent simultaneity, but they do not establish whether the vortex directly drives the observed dynamics. For instance, in the long-lived supergranular vortex studied by Requerey et al. (2017); Chian et al. (2022), the intensification and stabilization of a magnetic network element were observed to occur alongside vortex formation, but no formal causal analysis was performed. Consequently, these studies leave open key questions: Do vortices causally modulate heating or magnetic structuring, or are they simply co-evolving features responding to a common driver?

In this study, we used IT tools to investigate a solar tornado captured in a 3D simulation of a coronal hole. Our goal is to go beyond visual associations and directly measure how key physical variables interact over time. IT tools, though only recently introduced to space plasma studies, have proven transformative in uncovering hidden structure and causality in nonlinear systems. Unlike traditional correlation-based diagnostics, IT methods can identify directionality and time-lagged interactions in turbulent multiscale environments. For example, transfer entropy has been used to show that solar flares may influence the timing of subsequent flaring events (Snelling et al. 2020), and to quantify how solar wind variability drives magnetospheric and radiation belt responses (Wing & Johnson 2019). More recently, IT has revealed vortex–flow coupling in turbulent plasmas (Yatomi & Nakata 2025), capturing causal pathways and scale-to-scale information transfer missed by conventional approaches. By computing both Shannon Entropy and normalized mutual information NMI, we are able to quantify, for the first time, the complexity of the dynamics in a simulated solar tornado and the strength of the coupling between vorticity and key MHD variables during the vortex flow lifecycle. We performed the same analysis in a region with a magnetic flux tube

that did not support a solar tornado. This approach allows us to address several open questions: What mechanisms dominate the thermal evolution within large-scale solar vortices? How do magnetic shear and vorticity evolve during vortex formation and decay? Are heating processes localized and dynamic, or diffuse and passive? And, critically, can we separate correlation from causation in vortex-driven energy transfer? Through this lens, we demonstrate that magnetic structuring and current-related quantities are persistently and causally linked to plasma heating, particularly during the vortex phase. The enhanced statistical coupling in the vortex region, contrasted against a control case without a vortex, further emphasizes the dynamic and localized nature of these processes. The methods presented here provide a general framework for applying information theory to both simulations and observations of the solar atmosphere, offering new tools for diagnosing energy transport in highly nonlinear and data-limited environments.

We show that entropy increases and coupling patterns in the vortex region are consistent with magnetic complexity and dynamic interactions. The persistent NMI between temperature and magnetic shear during the vortex phase highlights current-driven heating as a dominant mechanism. Importantly, these coupling signatures vanish before and after the vortex event, confirming their dynamic origin. Our results establish IT diagnostics as powerful tools for probing causality and heating in nonlinear plasma environments and offer a path forward for future studies using simulations or limited observational datasets.

2. METHODS

2.1. Numerical Model: Bifrost simulation

The simulation analysed in this study is dataset `ch024031_by200bz005`, produced using the `Bifrost` code (Gudiksen et al. 2011). The `Bifrost` code is a 3D radiative magnetohydrodynamics (MHD) model that captures the coupled dynamics of the solar convection zone, photosphere, chromosphere, transition region, and lower corona within a single, self-consistent framework. The analysed dataset consists of a vertically extended, low-density corona with a magnetically open topology. Thus, it captures key signatures of coronal holes, including reduced EUV emission and vertical magnetic connectivity. This simulation has also been used in earlier studies to examine vortex dynamics (Silva et al. 2024b; Finley, A. J. et al. 2022). The simulation domain spans $24 \times 24 \times 16.8$ Mm³, resolved with 768^3 grid points, and extends from 2.5 Mm below the solar surface (defined at optical depth unity, $z = 0$ Mm) up to 14.3 Mm into the corona. The lower boundary in-

cludes a steady horizontal magnetic inflow, injecting a uniform field of 5 G, superimposed on a net vertical field of 200 G. The simulation setup creates a strongly unipolar magnetic environment with open field lines. The upper boundary is open, and energy balance is handled through full radiative transfer in the lower atmosphere. This includes non-LTE scattering (Carlsson & Leenaarts 2012), optically thin radiative losses, anisotropic thermal conduction, and ambipolar diffusion.

From the full simulation domain, we selected two subregions of $6 \times 6 \text{ Mm}^2$ in the horizontal plane. One region hosts a solar tornado. This structure has been previously analyzed in detail by Silva et al. (2024b). The second region contains only a vertical magnetic flux tube and serves as a control region with no dominant vortical motion. To place the vortex analysis in spatial context, Figure 1 shows the full horizontal extent of the BIFROST simulation, colored by the vertical magnetic field component B_z at a height of 2 Mm. The two selected subdomains are indicated by the black and red squares. The black square marks the region containing the large-scale, long-lived vortex, while the red square denotes the nearby control region. These contrasting subdomains allow us to assess the influence of vortex dynamics on the evolution of magnetic structure and plasma variability.

2.2. Dynamic Masking and Spatial Focus

To isolate the dynamics local to the kinetic vortex, we applied a spatial mask that is automatically tracking the evolving flux tube through height and time. The mask was defined as a circular region of fixed physical radius (in Mm), applied to each horizontal xy -slice of the vortex region. This mask served to limit all statistical calculations, namely SE, NMI, to the immediate neighborhood of the vortex core. The mask center was automatically determined for each height and time step as follows:

1. At each height, we identified the location of maximum magnetic field strength ($|\mathbf{B}|$) within the selected field of view. This point marks the central axis of the magnetic flux tube.
2. We placed a circular mask of fixed radius centered on this point. To capture both the photospheric and chromospheric parts of the vortex, each with different horizontal sizes, we chose a compromise radius of 0.5 Mm that ensures consistent coverage across heights.
3. To keep the mask aligned vertically, we set a limit on how much it could shift between height layers.

If the new center moved more than two pixels from the one below it, we keep the old position instead. This helped to avoid jumping to nearby features or noise. We used the same rule when tracking the mask over time.

We ran this tracking method automatically across all time steps and heights, effectively building a 3D cylindrical region that follows the magnetic flux tube over time. Although vorticity was also computed, it was not used to define the tracking path. Magnetic flux concentrations appear before the vortex forms and remain after it fades, making them a more consistent reference. This approach also lets us compare regions with and without strong vortex activity to better isolate the effects of coherent rotation. An example of the selected region at 500 seconds and 3 Mm height is shown in Figure 2, with red arrows marking the direction of the velocity field and the location of the mask.

2.3. Information Theory Quantification

To understand how plasma properties vary and interact within the vortex, we applied IT tools to several physical variables, including the vertical magnetic field (B_z), total magnetic field strength ($|B|$), vertical velocity (v_z), vorticity, temperature, density, and pressure. The first of these tools is Shannon entropy, which, in this context, quantifies the spatial variability or disorder of a physical quantity. A high entropy value indicates strong spatial fluctuations, pointing to a complex or possibly turbulent structure. In contrast, low entropy implies greater spatial uniformity, reflecting a more coherent or stable region.

Physically, high entropy in B_z or $|B|$ suggests that the magnetic field is highly structured, possibly due to twisting, braiding, or the formation of current sheets. Low entropy in these quantities indicates an organized field, as seen in magnetically dominated regions or within stable flux tubes. For velocity and vorticity, high entropy reflects disordered or fine-structured flows. This can arise from turbulent motions or from overlapping wave modes, such as Alfvén or magnetoacoustic waves, which introduce spatial variability as they propagate through the magnetized plasma. When applied to thermodynamic variables such as temperature, density, and pressure, high entropy indicates significant spatial gradients and inhomogeneity—often associated with localized heating, shocks, or dynamic flows. Conversely, low entropy in these fields suggests more uniform conditions, typical of equilibrium or quasi-static regions.

In the mask region, each variable was normalized prior to histogram construction to ensure consistency across heights and time steps. To calculate entropy, we divide

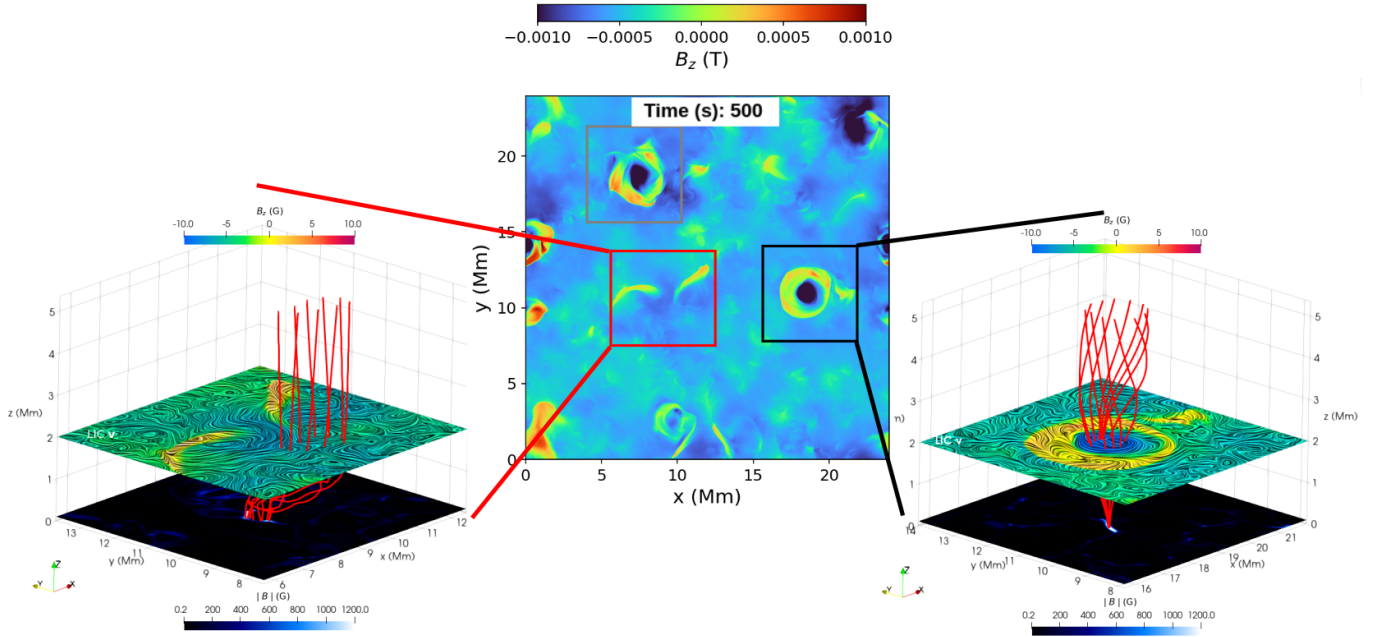


Figure 1. Central panel: Full horizontal extent of the BIFROST simulation domain at $t = 500$ s, showing the vertical magnetic field component B_z at a height of 2 Mm. The two analyzed subregions are marked by the red and black squares, respectively. **Left panel:** 3D view of the region without large-scale vortical activity. Red lines indicate selected magnetic field lines seeded near the center of the subdomain. The horizontal slice at $z = 2$ Mm is colored by B_z , with line-integrated convolution (LIC) patterns overplotted to reveal the horizontal velocity field. The bottom slice at the photosphere ($z = 0$ Mm) also shows B_z for context. **Right panel:** Same as left, but for the region containing the dynamically tracked large-scale kinetic vortex. The LIC texture highlights the coherent rotational motion, and the magnetic field lines reveal a twisted, vertically extended structure anchored in the vortex core.

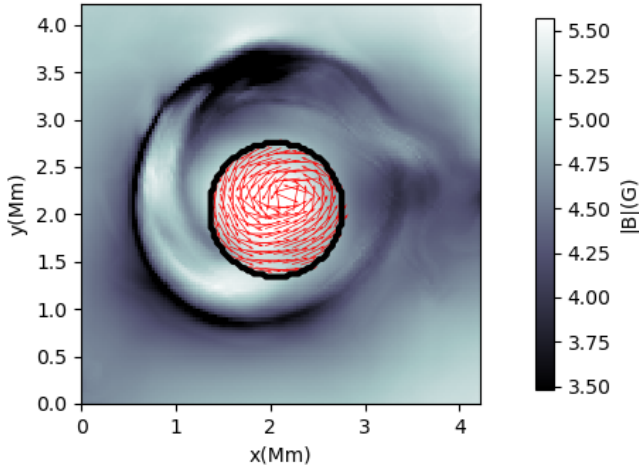


Figure 2. Magnetic-field magnitude $|B|$ (grayscale, in Gauss) with unit velocity vectors (red) shown inside the circular mask (black contour) that automatically identifies the vortex region at $z = 3$ Mm and $t = 500$ s

the variable range into bins K and calculate the empirical probability p_i as the fraction of grid cells that fall into the bin i . The entropy was then computed in bits

using a logarithmic base $b = 2$

$$H = - \sum_{i=1}^K p_i \log_2 p_i. \quad (1)$$

We tested both adaptive and fixed binning approaches. Adaptive binning adjusts to the local spread of the data, but it often over-resolved the histogram in regions with narrow distributions or limited sample sizes. This resulted in nearly uniform probability distributions and artificially high entropy values, which washed out spatial and temporal contrasts in the entropy maps. Fixed binning, on the contrary, preserved coherent structures and transitions across all variables and more clearly reflected known dynamic processes, such as vortex emergence and decay. For this reason, we adopt the fixed binning as the more interpretable and physically consistent method.

2.3.1. Coupling analysis using MI

MI is built on the same foundations as entropy, making it a powerful tool for uncovering relationships between variables. In both physics and information theory, entropy measures uncertainty or disorder. When two variables are related, knowing one reduces the uncertainty in the other. MI quantifies this reduction, not

through assumptions about the type of relationship, but through the amount of shared information. This makes MI sensitive to both linear and nonlinear connections, even when other methods like correlation fail to capture them. Since it is rooted in entropy, a core idea in both thermodynamics and information theory, MI offers a broadly applicable and physically meaningful way to measure dependence between quantities.

Because MHD systems are inherently nonlinear, traditional correlation-based measures may miss subtle, but important dependencies. MI, however, is sensitive to the full spectrum of possible interactions. To compare how strongly different pairs of variables are connected, or how this connection changes across heights or times, MI is often normalized. This places all variable comparisons on a common scale, making it possible to assess the relative strength of interactions in a consistent manner. Normalization can be done by dividing by the joint entropy, or by the geometric mean of the individual entropies. The result is a number between 0 and 1, where 0 means no shared information, and 1 means complete dependence. For example, a normalized MI value of 0.1 means that the two MHD variables share 10% of their total uncertainty. Put differently, knowing the state of one variable reduces uncertainty about the other by that fraction. In practical terms, a normalized MI above 0.1 indicates a nontrivial statistical dependency. For MHD, this can reveal meaningful coupling between physical processes, such as energy transfer across fields, cross-scale interactions in turbulence, or correlations between magnetic and velocity structures that would not necessarily be visible in linear measures. Thus, even a seemingly “small” MI value may signify deep physical connections in the dynamics of the plasma.

For two random variables X and Y their MI, $I(X; Y)$, is defined as

$$I(X; Y) = H(X) + H(Y) - H(X, Y). \quad (2)$$

Here, $H(X, Y)$ denotes the *joint entropy* between variables X and Y , which quantifies the total uncertainty associated with their combined outcomes. It reflects not only the individual variability of each variable, but also its shared structure. We normalized $I(X; Y)$ to account for differences in the marginal entropies of X and Y . The normalised MI (NMI) is defined as

$$\text{NMI}(X, Y) = \frac{I(X; Y)}{\sqrt{H(X)H(Y)}}. \quad (3)$$

Before computing the NMI, each variable was rescaled to a fixed range, either $[0, 1]$ or $[-1, 1]$, depending on its physical bounds. Joint histograms were then constructed using 64 uniformly spaced bins across the normalized range. This fixed binning approach provides

enough resolution to capture nonlinear dependencies while maintaining numerical stability in the mutual information estimates. Normalizing and binning in this way ensures consistency across variables and time steps, allowing for reliable comparisons and minimizing sensitivity to outliers or local fluctuations in the data.

To assess the statistical reliability of the observed information-theoretic coupling, we performed pixel-shuffle surrogate tests on each time–height window. For each driver–target pair, we generated $N = 500$ spatial surrogates by randomly permuting pixel positions within the vortex mask, which preserves marginal distributions while destroying spatial structure. For MI, we computed a null distribution and defined the p -value as the fraction of surrogates with values greater than or equal to the observed coupling. Across the entire analysed region and time interval, observed values exceeded all surrogate samples, yielding p -values $\lesssim 0.002$ in nearly all pixels. To further quantify the strength of the signal relative to surrogate variability, we computed the effect size as the absolute difference between the observed and mean surrogate values, and defined the signal-to-noise ratio (SNR) as $(\text{value}_{\text{obs}} - \mu_{\text{null}})/\sigma_{\text{null}}$. The resulting SNR maps show extended regions with values exceeding 5, and effect sizes well above the surrogate standard deviation. These metrics demonstrate that the observed couplings are not only statistically significant but also meaningfully stronger than surrogate-induced fluctuations, providing robust evidence of structured dependencies in the analysed regions.

RESULTS

To characterize the temporal and vertical evolution of physical conditions within the vortex, we computed time–height maps of spatially averaged quantities inside the tracked the magnetic flux tube core. By analyzing these averaged fields across the different vortex phases, before onset, development, and decay, we identify the signatures of dynamic coupling and energy concentration associated with vortex-driven activity. Figure 3 shows the temporal and variation with height of the vorticity of horizontal velocity (v_h), vertical velocity (v_z) and the base-10 logarithm of the spatially averaged values for each variable within the vortex core. The coloured stars indicate key stages in the vortex evolution as determined by the Γ -method (Graftieaux et al. 2001; Giagkiozis et al. 2018; Yuan et al. 2023), using the condition $\Gamma_1 > 0.66$ in the magnetic flux tube mask to define coherent rotation. We choose a lower value as initially the velocity field is not as twisted, leading to a lower Γ_1 . Blue stars mark the onset of the main vortex at each height, while orange stars indicate the end of

that initial coherent structure. As the main vortex decays, it fragments into smaller secondary vortices that persist for a time before fully dissipating; their presence is marked by green stars. The vortex appears to form between the high photosphere (approximately 0.45 Mm) and the low chromosphere (around 1.0 Mm), after which it expands both upward into the corona and downward toward the solar surface. In the upper atmosphere, the vortex decays into multiple smaller structures, whereas in the lower layers it disappears more abruptly. In particular, smaller vortices are more persistent around 2 Mm, indicating that vortex evolution may be stratified with height, with different lifetimes and dynamics depending on atmospheric depth.

The onset of the main vortex leaves identifiable signatures across all plasma variables, particularly in the chromosphere and transition region (heights above ~ 1.0 Mm). In the upper atmosphere, a reversal in the sign of the horizontal vorticity is observed around the time of vortex formation. This indicates a transition from small-scale, network-like flows exhibiting clockwise rotation into a dominant large-scale vortex rotating in the counterclockwise direction. The positive vorticity associated with the large-scale structure persists through most of the vortex's lifetime but gradually weakens as the coherent rotation breaks down. During the decay phase, the vortex transitions into smaller, fragmented swirling motions. This evolution reflects a redistribution of angular momentum and suggests a transfer of energy from organized, large-scale flows into localized, potentially dissipative motions.

One of the most prominent features is a sharp and sustained drop in plasma- β , which falls below unity shortly after vortex formation and remains low ($\log_{10}\beta \lesssim -1$) as long as coherent vortical structures persist. This behaviour marks a transition from a gas-pressure-dominated to a magnetically dominated regime. Simultaneously, both the kinetic and magnetic energy increase by over an order of magnitude, peaking near vortex's half-life. A local minimum in the vertical magnetic field B_z coincides with the onset of the main vortex (blue stars). This may reflect either a redistribution of magnetic flux by the swirling plasma motions, or the conversion of vertical field into horizontal components as the vortex twists and shears the local field. The subsequent increase in B_z indicates magnetic flux accumulation within the vortex core as it matures.

The formation of the vortex is accompanied by a coherent upflow of material, which transports denser plasma from lower atmospheric layers into the vortex core. This upflow results in a localized enhancement of mass density and a simultaneous drop in temperature,

consistent with adiabatic expansion and the lifting of a cooler, denser plasma. Throughout the lifetime of the vortex, upward velocities dominate within the core region, continuously transporting plasma from lower layers and sustaining the elevated density. This persistent upflow plays a crucial role in maintaining the mass loading of the vortex structure. Only toward the end of the vortex's life does this trend reverse, with downflows gradually becoming more prominent. This culminates in a strong downward jet along the vortex axis during its final decay phase, particularly in the upper atmospheric layers. The gas pressure initially increases at heights above 1.5 Mm as the upflow develops, but subsequently drops as the vortex matures. Following the initial cooling phase, the plasma within the vortex core is gradually heated, reaching temperatures up to an order of magnitude higher than the onset vortex state.

2.4. Tracking Plasma Coupling and Coherence via Information Theory

The profiles presented in Figure 3 characterize the background evolution of the vortex core and provide a reference context to interpret subsequent information-theoretic and structural analyzes. We computed SE to quantify the local spatial variability of key physical quantities within the tracked magnetic flux tube where the solar tornado is developed. Figure 4 shows the temporal and vertical evolution of the SE for the same variables as Figure 3, except for plasma- β . The entropy was computed within the dynamically tracked vortex core, and each panel presents the entropy values, revealing how the spatial organization and complexity of the plasma change over time and height. In practice, entropy values near $H \sim 2-3$ correspond to relatively ordered fields with low spatial variability, while intermediate values ($H \sim 4-5$) indicate partially structured states where coherent features coexist with moderate fluctuations. Higher values approaching $H \sim 6$ reflect strongly intermittent fields, likely associated with turbulence, sharp spatial gradients, or enhanced small-scale variability. The entropy was estimated from the empirical probability distributions at each height and time step using a fixed binning scheme of 64 bins.

The onset and development of the main vortex are marked by significant changes in the spatial organization of magnetic fields, as captured by entropy diagnostics. During the formation phase, the entropy of magnetic energy (E_{mag}) rises in the lower atmosphere, indicating increasing spatial complexity and localized structuring of the field. This is accompanied by a divergence between the entropy of E_{mag} and that of magnetic shear ($|\nabla \times \mathbf{B}_h|$), consistent with the formation of

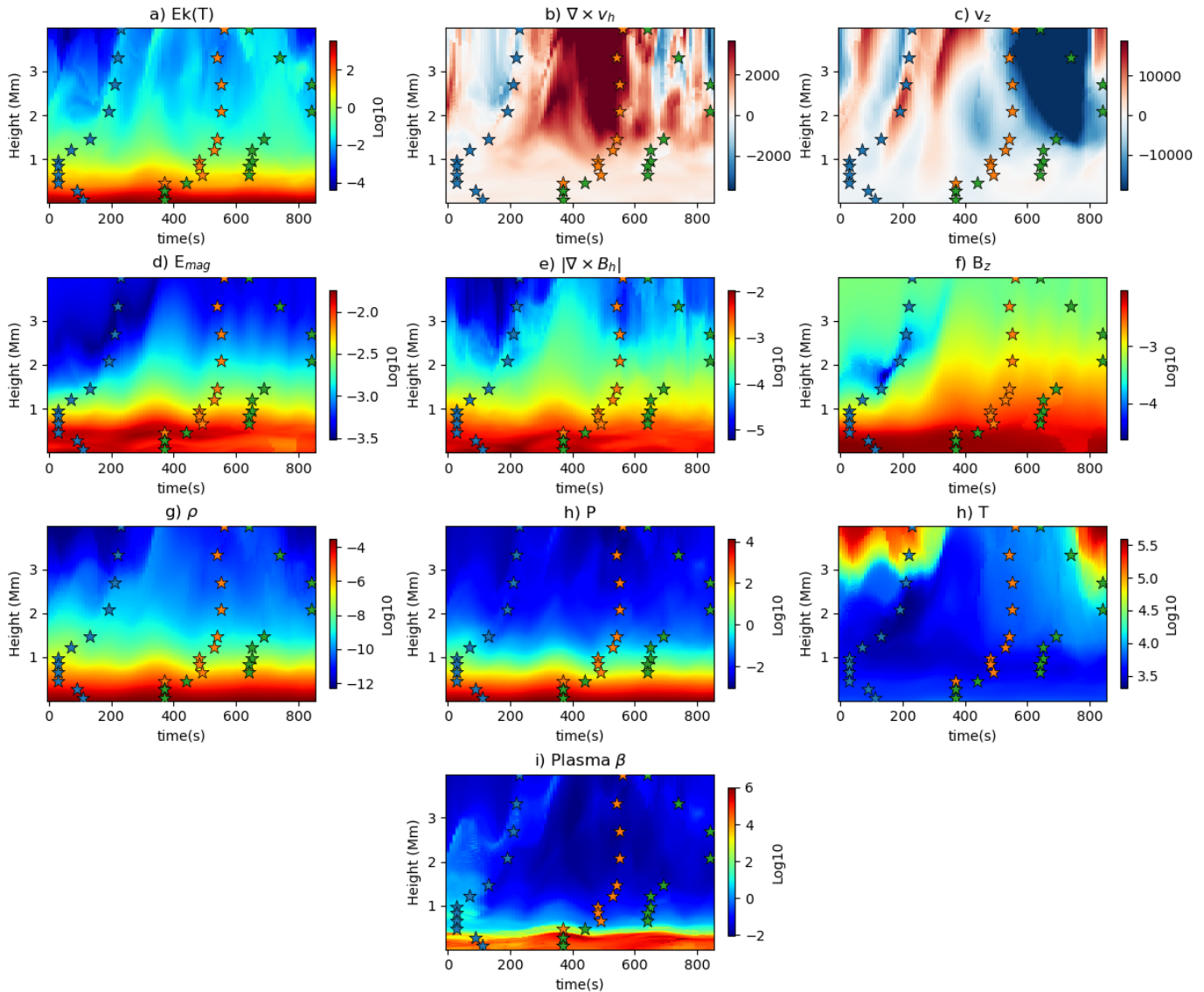


Figure 3. Temporal and vertical evolution the spatially averaged plasma quantities within the dynamically tracked magnetic flux core. Each panel corresponds to a different physical variable: (a) kinetic energy E_K , (b) horizontal vorticity $\nabla \times \mathbf{v}_h$, (c) vertical velocity v_z , (d) magnetic energy density E_{mag} , (e) transverse magnetic shear $|\nabla \times \mathbf{B}_h|$, (f) vertical magnetic field B_z , (g) mass density ρ , (h) gas pressure P , (i) temperature T , and (j) plasma- β . All variables are shown in base-10 logarithmic scale, except for the horizontal vorticity $\nabla \times \mathbf{v}_h$ and the vertical velocity v_z . Blue stars mark the onset of the main large-scale vortex, solar tornado, at each height, while orange stars indicate its decay. Green stars denote the termination of smaller secondary vortices that form after the decay of the primary structure. All times and locations were identified using the Γ -method with $\Gamma > 1$.

current sheets rather than uniform shear enhancement. While E_{mag} becomes more intermittent due to twisting and compression by the vortex, magnetic shear entropy remains vertically patchy and fragmented, suggesting that complexity arises from thin, spatially confined features rather than widespread braiding. Similarly, the entropy of the vertical field component (B_z) increases during the vortex onset—likely reflecting enhanced intermittency as flux elements are swept into the vortex—but later drops sharply between 1.5–3 Mm once the coher-

ent structure is established. This entropy reduction suggests that the vortex acts to stabilize and organize B_z , possibly through magnetic tension and vertical realignment. Prior to the onset of the vortex, both the magnitude and entropy of horizontal vorticity remain low in the upper atmosphere. This indicates a quiescent, non-rotational flow regime with minimal spatial variation, consistent with an irrotational, magnetically dominated background. The absence of pre-existing shear or turbulence suggests that the vortex did not arise from the

gradual accumulation of small-scale swirling motions or steady twisting of field lines. Instead, it likely formed abruptly in response to a localized, possibly impulsive, event, potentially triggered by plasma or magnetic instabilities. The entropy of the kinetic energy (E_K) increases with vortex onset, decreasing immediately after, reflecting the emergence of coherent flow patterns. However, this trend reverses near the vortex’s half-life, where entropy increases significantly. This delayed rise is likely driven by the emergence of shear flows that act to destabilise the coherent vortex and inject kinetic complexity into the system. Notably, this entropy growth in E_K is followed by a corresponding increase in the entropy of horizontal vorticity, which had been suppressed during the organised vortex phase. The subsequent increase in vorticity entropy marks the transition to a fragmented regime dominated by small-scale, disordered vortical structures, consistent with the formation of secondary swirls.

Temperature and pressure both exhibit an initially high entropy in the lower atmosphere, reflecting significant spatial variability prior to vortex formation. As the vortex emerges, entropy in both quantities decreases. Notably, pressure entropy drops more rapidly than temperature entropy, indicating that the pressure field becomes ordered earlier, possibly due to the propagation of magnetoacoustic waves that redistribute pressure more efficiently than thermal energy. Following this initial organisation phase, the two variables diverge in behaviour. The pressure entropy remains low throughout the middle and upper atmosphere during the lifetime of the vortex, with only a modest increase near the footpoints and below 1 Mm. In contrast, temperature entropy begins to rise in the upper atmosphere as the vortex develops, pointing to the formation of fine-scale thermal structure likely driven by localised heating and dynamic mixing processes. This growing thermal complexity aligns with the evolution of plasma temperature shown in Figure 3, where the vortex core heats significantly during its mature phase, while pressure remains relatively stratified and stable in the same region.

Figure 5 displays the evolution of the entropy in a control region without coherent vortex activity. A striking feature is the presence of vertically coherent, quasiperiodic fluctuations across several plasma variables, particularly in density, pressure, and temperature. These patterns likely reflect global p-mode oscillations driven by the lower boundary of the Bifrost simulation, which imposes perturbations to emulate solar acoustic modes. Interestingly, such periodic signatures are suppressed in the vortex region (Figure 4), suggesting that the presence of the vortex disrupts or decouples the propagation

of these global oscillations. Notably, previous studies using the same simulation have identified magnetoacoustic waves propagating within the vortex core, particularly in the lower atmosphere. Thus, these waves, are likely generated or modulated by the vortex itself, rather than inherited from the bottom boundary.

2.4.1. Linear and nonlinear coupling

To explore the degree of statistical dependence between rotational motion and key plasma parameters during the vortex lifecycle, we computed the NMI between the vorticity magnitude of horizontal plasma flow ($|\nabla \times \mathbf{v}_h|$) and each relevant physical quantity as displayed in Figure 6. Here, MI values are normalized to fall between 0 (no statistical dependence) and 1 (perfect dependence). NMI in Figure 6 ranges from 0 to approximately 0.4, providing a dimensionless measure of statistical dependence between vertical vorticity and each plasma variable. Values close to 0 indicate little to no shared information, reflecting largely uncorrelated or independent behavior. Moderate NMI values (0.1–0.25) suggest partial coupling, where the variable exhibits some degree of organization influenced by the vorticity field, possibly through indirect or non-linear interactions. Higher NMI values (approaching 0.3–0.4) correspond to stronger statistical dependence, reflecting coordinated evolution. The panels reveal that, during the vortex’s lifetime, the coupling between vorticity and several thermodynamic and magnetic variables is locally enhanced, particularly in the upper atmosphere. This behaviour contrasts with the more uniform and subdued NMI patterns observed in the no-vortex control region (Figure 7), confirming that the enhanced coupling in the vortex core is dynamically driven rather than arising from static background structure. In other words, the elevated NMI between rotational flows and thermodynamic variables reflects genuine physical interaction associated with vortex dynamics, rather than a spurious correlation due to their co-location within the same magnetic flux tube.

In the non-large-scale vortex region, where only small-scale swirling flows are present, NMI values remain generally low and spatially diffuse (Figure 7) in the upper atmosphere. This suggests a weak statistical coupling between vorticity and other plasma variables when coherent, vertically extended rotational structures are absent. The elevated NMI between temperature, v_z , and vorticity in the photospheric control region likely arises from granular-scale convection, intergranular downflows, and p-mode-induced oscillations, all of which structure the plasma in ways that naturally correlate temperature, vertical motion, and rotational

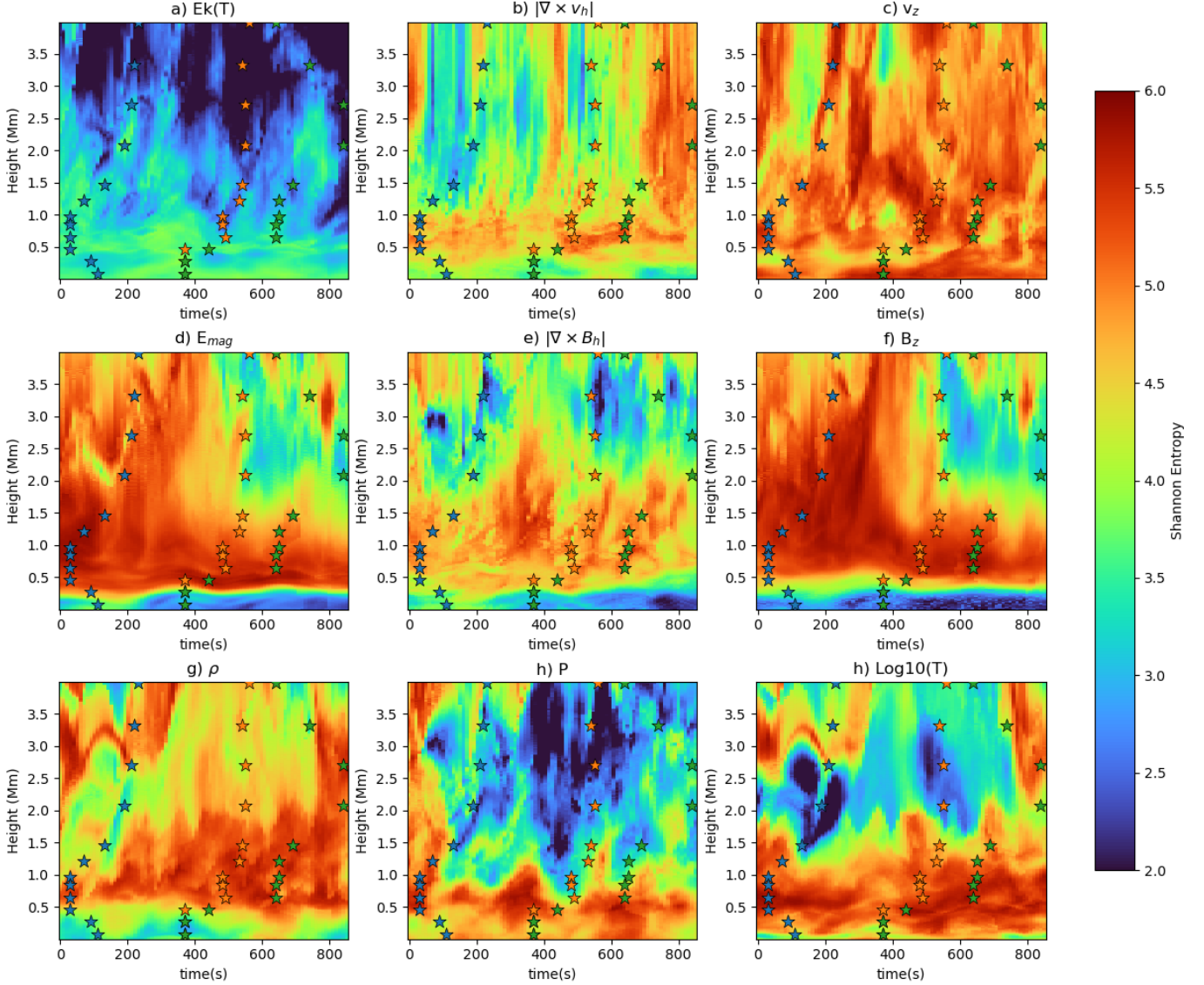


Figure 4. Temporal and vertical evolution of the Shannon entropy for various plasma variables, computed within the dynamically tracked vortex core. Entropy is estimated from the empirical probability distribution of each variable at every height and time, using fixed binning (64 bins). Each panel corresponds to a distinct quantity: (a) kinetic energy based on temperature, $E_K(T)$ (b) horizontal vorticity $\nabla \times \mathbf{v}_h$, (c) vertical velocity v_z , (d) magnetic energy E_{mag} , (e) transverse magnetic shear $|\nabla \times \mathbf{B}_h|$, (f) vertical magnetic field B_z , (g) mass density ρ , (h) gas pressure P , and (i) temperature T . Blue and orange stars mark the onset and end of the large-scale vortex, while green stars indicate the disappearance of secondary vortex structures

shear—even in the absence of a coherent vortex. Importantly, a low vorticity amplitude does not necessarily imply a low NMI, nor does a high vorticity guarantee strong coupling. What NMI captures is not the intensity of a given quantity, but the degree to which two variables co-vary in a structured and predictable manner. The persistently lower NMI in this control region reinforces the idea that strong mutual dependence, as seen in the vortex core, requires not just vorticity, but organized dynamics capable of modulating the surrounding plasma fields.

2.5. Plasma heating

To identify the key drivers of temperature evolution within the vortex, we computed the NMI between plasma temperature and a selection of physical variables linked to heating processes or thermodynamic coupling. Figure 8 presents the temporal and vertical variation of these dependencies within the vortex core. The initial enhanced coupling between v_z , $\nabla \cdot \mathbf{v}_h$ and temperature is most pronounced during the vortex development and in the lower atmosphere, suggesting that the initial plasma cooling is driven by the jet transporting the

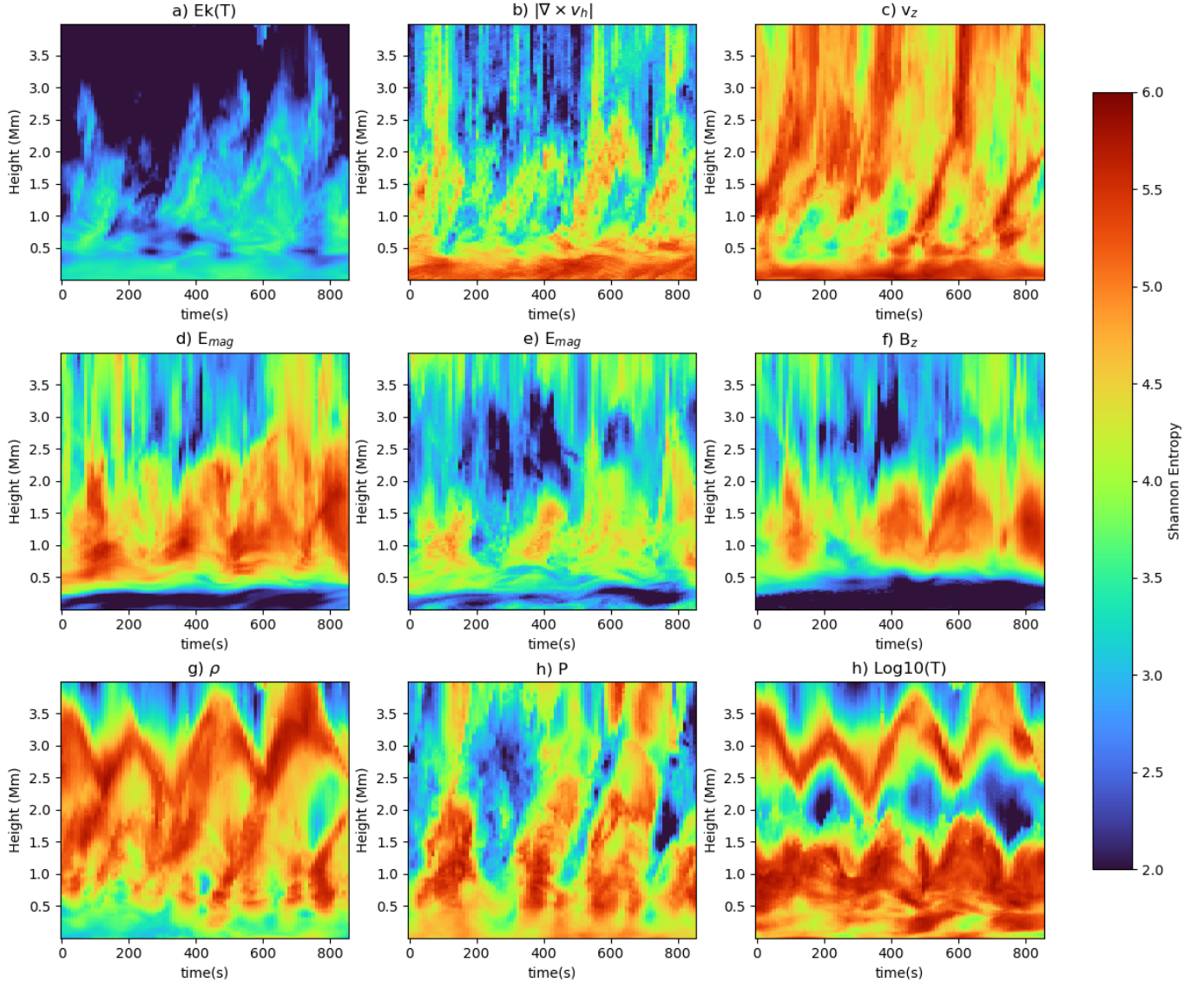


Figure 5. Same as Figure 4, but for a region without vortex activity. The entropy evolution shows clearer periodic patterns, particularly in pressure and density, likely due to p-mode-like wave injection from the bottom boundary in the simulation.

vortex upwards and the initial flux tube expansion. As expected, plasma temperature initially shows strong statistical coupling with both density and pressure, consistent with the ideal gas law under quasi-static conditions. However, during the vortex phase, the coupling with plasma density significantly weakens above 1 Mm, indicating that the temperature evolution is no longer primarily governed by adiabatic compression or expansion. Instead, this points to a breakdown of ideal thermodynamic behavior due to non-adiabatic processes such as current dissipation, wave heating, and magnetically induced flows. The reduced NMI between temperature and density/pressure reflects the growing influence of magnetic forces and energy injection mechanisms in the upper atmosphere.

Although vortex-driven expansion initially leads to adiabatic cooling, this effect is short-lived. Within 10 time steps, the plasma temperature begins to rise, indicating that additional heating mechanisms rapidly become dominant. The sustained NMI between temperature and magnetic shear throughout the vortex lifetime suggests that current structures play a consistent role in modulating plasma heating. This coupling is particularly notable given that the magnetic shear–temperature association emerges primarily during the vortex phase, vanishing before and after. This timing supports the interpretation that currents, associated with twisted and evolving magnetic fields, contribute to localized heating within the vortex core. The temporal alignment between this temperature rise and elevated magnetic shear points

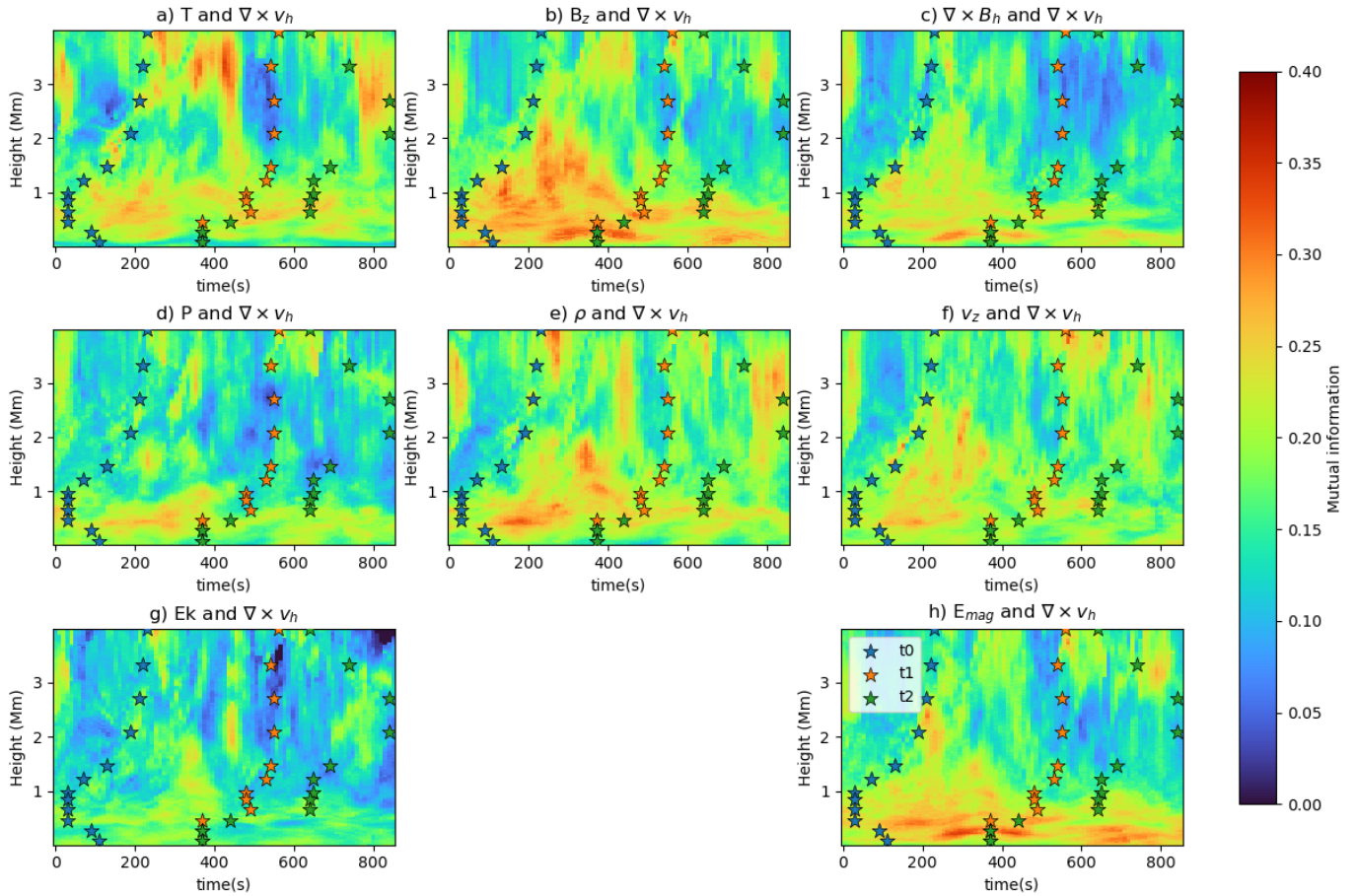


Figure 6. Temporal and vertical structure of the Mutual Information (MI) between the horizontal vorticity magnitude ($|\nabla \times \mathbf{v}_h|$) and various plasma quantities, computed within the dynamically tracked vortex core region. Different panels show MI between vorticity and: (a) temperature T , (b) vertical magnetic field B_z , (c) transverse magnetic shear $|\nabla \times \mathbf{B}_h|$, (d) gas pressure P , (e) density ρ , (f) vertical velocity v_z , (g) kinetic energy density E_K , and (h) magnetic energy density E_{mag} . MI values are shown in normalized units (bits), with warmer colors indicating stronger dependence. Stars denote key moments in the vortex evolution: blue for onset (t_0), orange for decay of the main vortex (t_1), and green for the dissipation of residual swirls (t_2).

toward current dissipation as a likely source of energy input. Although this dissipation is numerical in origin, because of the lack of explicit resistivity in the simulation, it still reflects the physical tendency for currents to form and dissipate in regions of strong shear. This supports the interpretation that vortex-driven magnetic structuring can channel energy into thermal heating, especially under the low plasma- β conditions of the chromosphere and transition region.

3. DISCUSSIONS AND CONCLUSION

We examine two large magnetic flux tubes: one that hosts a strong solar tornado with a coherent vortex flow and another characterized only by shear flows and transient swirls. The vortex flow first emerges in the upper photosphere and lower chromosphere. From there, it expands both upward and downward, forming a long-lived column of rotating plasma. It persists for approximately 5–10 minutes, with a horizontal radius of over 1 Mm in the upper atmosphere. Our analysis focuses on its evolution from the photosphere through the upper atmosphere, within the height range of 0–4 Mm. Throughout the full height of the vortex, the plasma- β steadily decreases as the structure develops, reflecting a growing dominance of magnetic forces over gas pressure. Interestingly, the magnetic field intensifies at the vortex onset and remains strong even after the large-scale structure dissolves, pointing to lasting magnetic reconfiguration as reported by [Díaz-Castillo, S. M. et al. \(2024\)](#). Aside from a brief initial cooling, the vortex phase is marked by a persistent temperature increase, highlighting the efficiency of heating mechanisms operating throughout its lifetime.

Using information-theoretic diagnostics, SE and NMI, we quantified how vortex evolution alters MHD interactions. SE captures changes in the spatial complexity of individual variables, while NMI highlights how their couplings strengthen or weaken over time and height. The magnetic field variables illustrate this complementarity. SE shows that the entropy of the vertical magnetic field rises during vortex onset in the upper atmosphere, indicating the development of stronger spatial gradients and irregular distributions of the vertical magnetic field. As the vortex matures, B_z entropy decreases, reflecting the emergence of a more ordered, collimated structure. By contrast, magnetic shear entropy begins low, rises sharply through vortex development as currents intensify, and falls again in the decay phase, consistent with current dissipation. Cross-comparison with NMI maps reveals that when magnetic shear entropy peaks, temperature becomes strongly coupled to shear, indicating that thermal evolution is linked to the

buildup and subsequent dissipation of current-related complexity.

The thermodynamic variables also show clear stratification. In the lower atmosphere, SE indicates low entropy in density but high entropy in pressure, reflecting relatively uniform mass loading alongside strong compressive variability. NMI confirms that temperature remains persistently coupled to horizontal compression ($\nabla \cdot v_h$) throughout the vortex lifetime. At the same time, temperature also shows strong coupling with vorticity, which itself contributes to velocity gradient. This dual dependence suggests that both compressive processes and viscous dissipation contribute to heating in the lower layers. In the upper atmosphere, the entropy patterns reverse: density entropy rises (stronger gradients and irregular distributions) while pressure entropy decreases (more ordered stratification). The coupling of temperature and density diminish considerably in the upper part of the domain, indicating departing from the ideal gas law. NMI reveals that temperature coupling with vorticity persists here, implying a continuing role for viscous heating, but now temperature also couples strongly to magnetic shear. This indicates that, higher up, magnetic structuring and current dissipation become additional drivers of thermal evolution alongside viscous effects. This confirms that vortices enhance the formation of both velocity and magnetic field gradients, creating favorable conditions for energy dissipation, consistent with previous studies ([Yadav et al. 2021](#); [Silva et al. 2024a,b](#)). Our analysis extends this picture by showing that plasma temperature is statistically coupled to these gradients, demonstrating that the dissipated energy is effectively converted into heating within the vortex. Although the simulation does not include explicit resistivity, the hyperdiffusivity terms act on sharp gradients in the magnetic and velocity fields. In practice, this mimics the effect of current and viscous dissipation, meaning that regions where the vortex generates strong shear or currents correspond to sites of effective energy release. Thus, the observed thermal signatures can be interpreted as an analogue of vortex-driven heating in the solar atmosphere.

The coupling is not one-sided: plasma variables also influence vorticity. Elevated temperature can enhance pressure gradients, which in turn drive flows that sustain or modify vortical motions. In the lower atmosphere, where pressure entropy is high, pressure gradients are likely to reinforce rotational shear and help maintain vortex coherence. In the upper atmosphere, strong magnetic shear can exert Lorentz forces that realign flows, thereby shaping or even destabilizing the vortex. The observed NMI links therefore suggest a

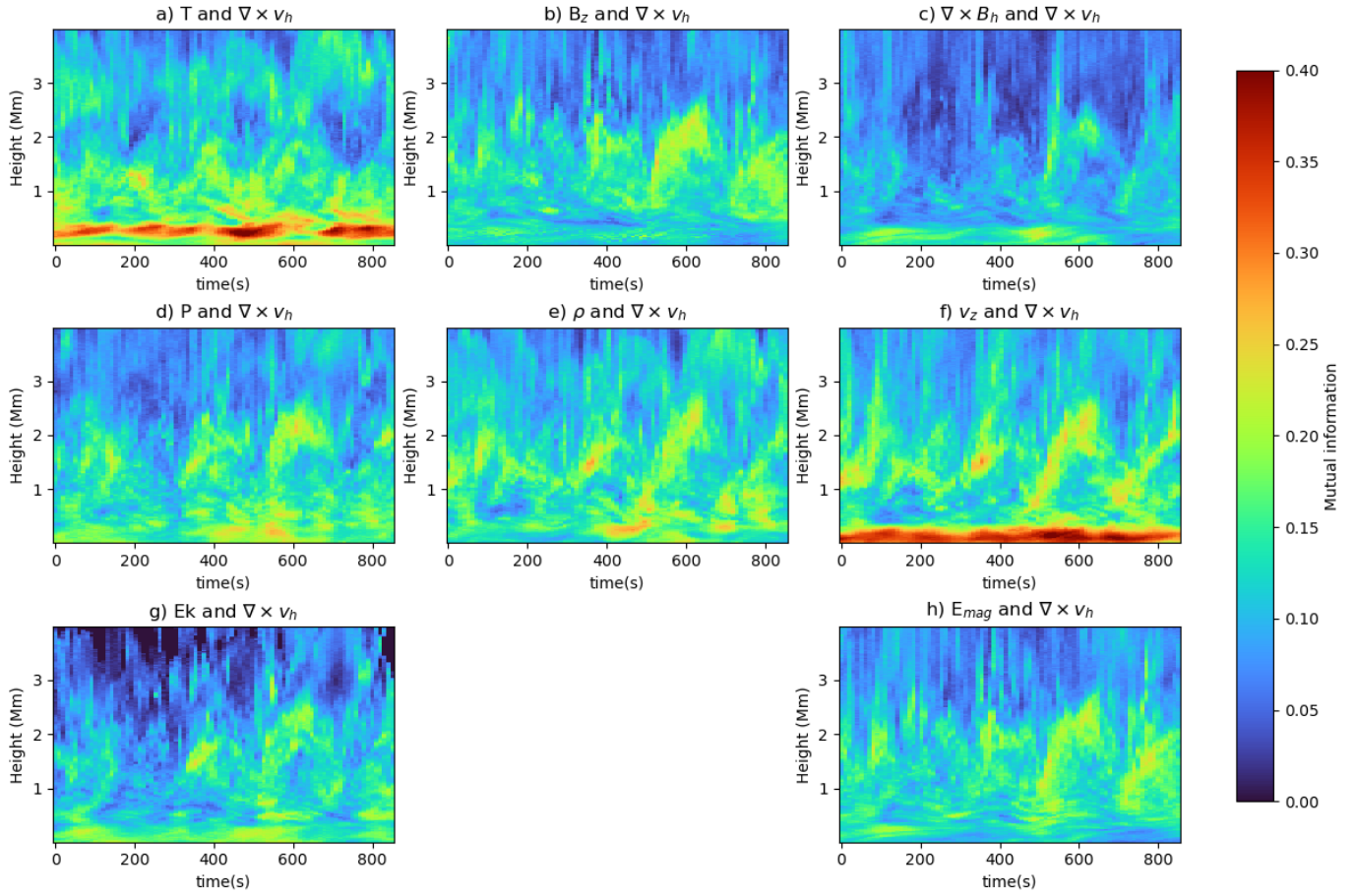


Figure 7. Same as Figure 6, but for a control region where no vortex is present, only a vertical magnetic flux tube.

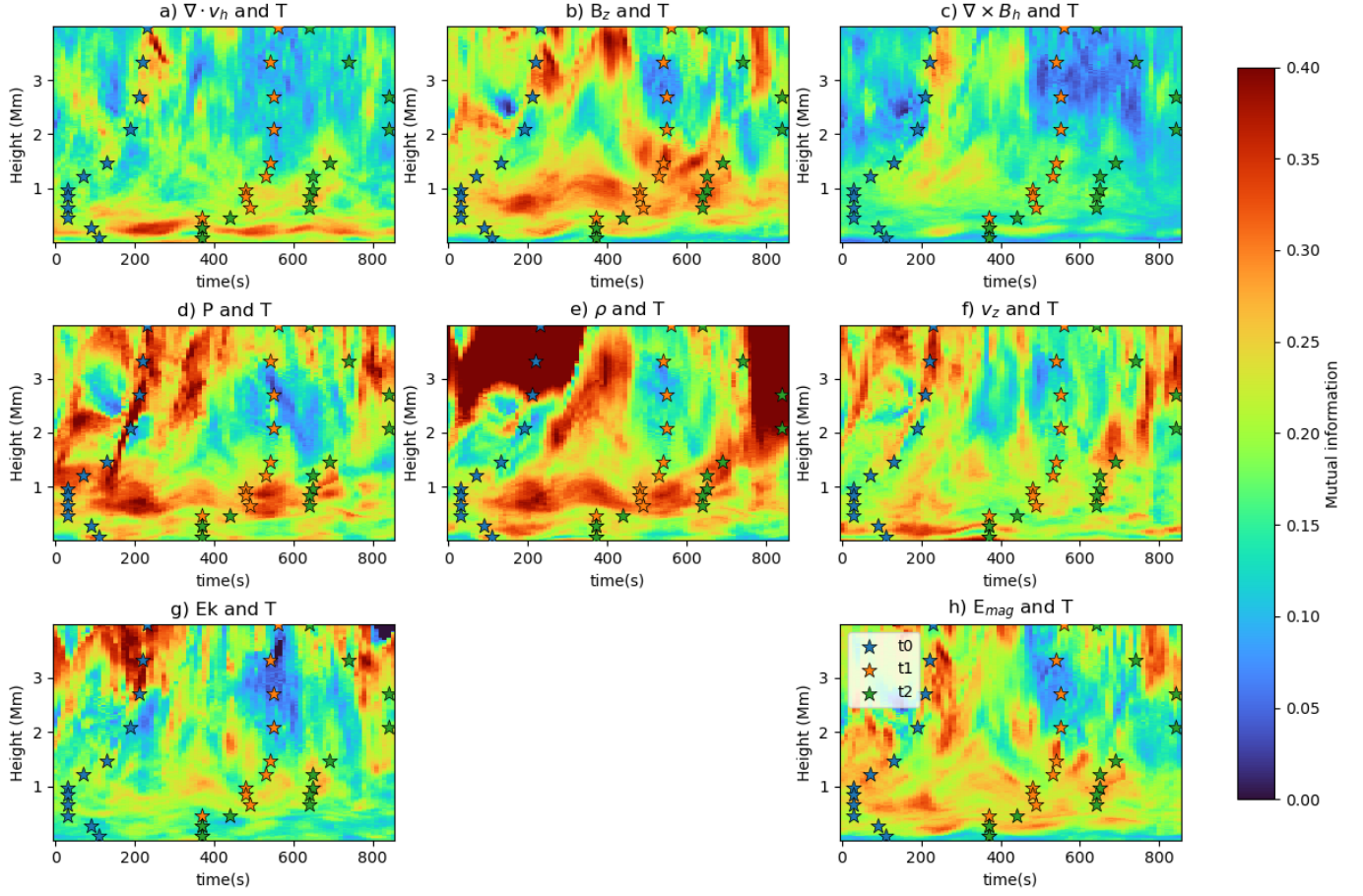


Figure 8. NMI between plasma temperature and other variables within the dynamically tracked vortex core region. Each panel shows the NMI between temperature and a different quantity: a) horizontal velocity divergence ($\nabla \cdot \mathbf{v}_h$), b) vertical magnetic field (B_z), c) transverse magnetic shear ($\nabla \times \mathbf{B}_h$), d) gas pressure (P), e) mass density (ρ), f) vertical velocity (v_z), g) kinetic energy density (E_K), and h) magnetic energy density (E_{mag}). Higher NMI values (red) indicate stronger statistical dependence. Blue, orange, and green stars denote the onset, end, and decay of the main vortex as identified by the Γ -method

bidirectional relationship: vorticity drives gradients that heat the plasma, while thermal and magnetic structuring provide feedback that regulates the strength, persistence, and eventual decay of the vortex as reported by (?Silva et al. 2024a)

The joint use of NMI and SE demonstrates that information theory provides a robust, flexible framework for probing nonlinear plasma interactions, even in data-limited settings. In particular, IT offers a pathway to assess causal dynamics without requiring full knowledge of the underlying governing equations. One of the major advantages of MI in plasma physics is that it bypasses some of the practical difficulties associated with working directly with the MHD equations. While the governing equations are complete in principle, in practice, they are highly nonlinear, coupled, and often intractable when one seeks to isolate the contribution of a specific process. Deriving the precise contribution of dynamic processes to plasma heating directly from the

MHD equations is highly nontrivial. To even express temperature evolution analytically, one must assume an ideal gas law and a single-fluid approximation. Such assumptions break down in partially ionized, radiatively active, and magnetically structured regions like the solar chromosphere and in the vortex itself, as showed by our results. The energy equation includes complex terms such as anisotropic thermal conduction, optically thick radiative losses, and nonlinear coupling between velocity, magnetic fields, and thermodynamic variables. These nonlinear, scale-coupled interactions make it extremely difficult to isolate causal drivers analytically or via direct term-by-term decomposition. In contrast, IT tools, like NMI, allow empirical quantification of statistical dependencies, without assuming specific forms of the governing equations. As high-resolution chromospheric observations continue to improve, IT diagnostics offer a practical and scalable tool set for interpreting complex magnetic structures such as vortices, swirls, or flux

ropes. Ultimately, these methods enable new ways to disentangle the drivers of plasma heating and energy transport in the solar atmosphere, and extend naturally to other astrophysical systems governed by turbulent, nonlinear dynamics.

ACKNOWLEDGMENTS

S.S.A.S. and V.F. are grateful to the Science and Technology Facilities Council (STFC) grants ST/V000977/1,

ST/Y001532/1. S.S.A.S., I.B., V.F. are grateful to The Royal Society, International Exchanges Scheme, collaboration with Greece (IES/R1/221095). E.L.R. acknowledges the Brazilian agency CNPq under grant 306920/2020-4. S.S.A.S. and V.F. would like to thank the International Space Science Institute (ISSI) in Bern, Switzerland, for the hospitality provided to the members of the team on ‘Opening new avenues in identifying coherent structures and transport barriers in the magnetised solar plasma’. S.S.A.S. is grateful to Iñaki Esnaola for insightful discussions that contributed to this work.

REFERENCES

- Carlsson, M., & Leenaarts, J. 2012, *Astronomy & Astrophysics*, 539, A39, doi: [10.1051/0004-6361/201118366](https://doi.org/10.1051/0004-6361/201118366)
- Chian, A. C.-L., Rempel, E. L., Silva, S. S. A., Bellot-Rubio, L., & Gošić, M. 2022, *Monthly Notices of the Royal Astronomical Society*, 518, 4930, doi: [10.1093/mnras/stac3352](https://doi.org/10.1093/mnras/stac3352)
- Chian, A. C. L., Silva, S. S. A., Rempel, E. L., et al. 2019, *Monthly Notices of the Royal Astronomical Society*, 488, 3076, doi: [10.1093/mnras/stz1909](https://doi.org/10.1093/mnras/stz1909)
- Cover, T., & Thomas, J. 2012, *Elements of Information Theory* (Wiley). <https://books.google.co.uk/books?id=VWq5GG6ycxMC>
- Dakanalis, I., Tsiropoula, G., Tziotziou, K., & Kontogiannis, I. 2022, *Astronomy & Astrophysics*, 663, A94, doi: [10.1051/0004-6361/202243236](https://doi.org/10.1051/0004-6361/202243236)
- Dakanalis, I., Tsiropoula, G., Tziotziou, K., & Koutroumbas, K. 2021, *Solar Physics*, 296, 17, doi: [10.1007/s11207-020-01748-3](https://doi.org/10.1007/s11207-020-01748-3)
- Díaz-Castillo, S. M., Fischer, C. E., Rezaei, R., Steiner, O., & Berdyugina, S. 2024, *Astronomy & Astrophysics*, 691, A37, doi: [10.1051/0004-6361/202349081](https://doi.org/10.1051/0004-6361/202349081)
- Fedun, V., Shelyag, S., Verth, G., Mathioudakis, M., & Erdélyi, R. 2011, *Annales Geophysicae*, 29, 1029, doi: [10.5194/angeo-29-1029-2011](https://doi.org/10.5194/angeo-29-1029-2011)
- Finley, A. J., Brun, A. S., Carlsson, M., et al. 2022, *A&A*, 665, A118, doi: [10.1051/0004-6361/202243947](https://doi.org/10.1051/0004-6361/202243947)
- Giagkiozis, I., Fedun, V., Scullion, E., Jess, D. B., & Verth, G. 2018, *The Astrophysical Journal*, 869, 169, doi: [10.3847/1538-4357/aaf797](https://doi.org/10.3847/1538-4357/aaf797)
- Graftieaux, L., Michard, M., & Grosjean, N. 2001, *Measurement Science and Technology*, 12, 1422, doi: [10.1088/0957-0233/12/9/307](https://doi.org/10.1088/0957-0233/12/9/307)
- Gudiksen, B. V., Carlsson, M., Hansteen, V. H., et al. 2011, *Astronomy & Astrophysics*, 531, A154, doi: [10.1051/0004-6361/201116520](https://doi.org/10.1051/0004-6361/201116520)
- Kuniyoshi, H., Bose, S., & Yokoyama, T. 2024, *The Astrophysical Journal Letters*, 969, L34, doi: [10.3847/2041-8213/ad5a0e](https://doi.org/10.3847/2041-8213/ad5a0e)
- Kuniyoshi, H., Shoda, M., Iijima, H., & Yokoyama, T. 2023, arXiv e-prints, arXiv:2304.03010, doi: [10.48550/arXiv.2304.03010](https://doi.org/10.48550/arXiv.2304.03010)
- Przybylski, D., Cameron, R., Solanki, S. K., et al. 2025, Structure and dynamics of the internetwork solar chromosphere: results of a small-scale dynamo simulation. <https://arxiv.org/abs/2508.19809>
- Requerey, I. S., Del Toro Iniesta, J. C., Bellot Rubio, L. R., et al. 2017, *The Astrophysical Journal Supplement Series*, 229, 14, doi: [10.3847/1538-4365/229/1/14](https://doi.org/10.3847/1538-4365/229/1/14)
- Silva, S. d. S. e. A., Rempel, E. L., Gomes, T. F. P., Requerey, I. S., & Chian, A. C.-L. 2018, *The Astrophysical Journal Letters*, 863, L2, doi: [10.3847/2041-8213/aad180](https://doi.org/10.3847/2041-8213/aad180)
- Silva, S. S. A., Fedun, V., Verth, G., Rempel, E. L., & Shelyag, S. 2020, *The Astrophysical Journal*, 898, 137, doi: [10.3847/1538-4357/ab99a9](https://doi.org/10.3847/1538-4357/ab99a9)
- Silva, S. S. A., Murabito, M., Jafarzadeh, S., et al. 2022, *The Astrophysical Journal*, 927, 146, doi: [10.3847/1538-4357/ac4601](https://doi.org/10.3847/1538-4357/ac4601)
- Silva, S. S. A., Verth, G., Ballai, I., et al. 2024a, *The Astrophysical Journal*, 975, 118, doi: [10.3847/1538-4357/ad781a](https://doi.org/10.3847/1538-4357/ad781a)
- Silva, S. S. A., Verth, G., Rempel, E. L., et al. 2024b, *The Astrophysical Journal*, 963, 10, doi: [10.3847/1538-4357/ad1403](https://doi.org/10.3847/1538-4357/ad1403)
- Silva, S. S. A., Verth, G., Rempel, E. L., et al. 2021, *The Astrophysical Journal*, 915, 24, doi: [10.3847/1538-4357/abfec2](https://doi.org/10.3847/1538-4357/abfec2)
- Snelling, J. M., Johnson, J. R., Willard, J., et al. 2020, *The Astrophysical Journal*, 899, 148, doi: [10.3847/1538-4357/aba7b9](https://doi.org/10.3847/1538-4357/aba7b9)
- Tziotziou, K., Scullion, E., Shelyag, S., et al. 2023, *Space Science Reviews*, 219, 1, doi: [10.1007/s11214-022-00946-8](https://doi.org/10.1007/s11214-022-00946-8)

Wedemeyer-Böhm, S., Scullion, E., Steiner, O., et al. 2012,
Nature, 486, 505, doi: [10.1038/nature11202](https://doi.org/10.1038/nature11202)

Wing, S., & Johnson, J. R. 2019, Entropy, 21, 140,
doi: [10.3390/e21020140](https://doi.org/10.3390/e21020140)

Yadav, N., Cameron, R. H., & Solanki, S. K. 2021,
Astronomy & Astrophysics, 645, A3,
doi: [10.1051/0004-6361/202038965](https://doi.org/10.1051/0004-6361/202038965)

Yatomi, G., & Nakata, M. 2025, Phys. Rev. Res., 7, 023212,
doi: [10.1103/PhysRevResearch.7.023212](https://doi.org/10.1103/PhysRevResearch.7.023212)

Yuan, Y., de Souza e Almeida Silva, S., Fedun, V.,
Kitiashvili, I. N., & Verth, G. 2023, ApJS, 267, 35,
doi: [10.3847/1538-4365/acc835](https://doi.org/10.3847/1538-4365/acc835)